Engineering spin absorption enables high spin orbit torque efficiency for fully electric-driven magnetization switching

Pengwei Dou,[#] Jingyan Zhang,[#*] Tao Zhu, Peng Kang, Xiao Deng, Yuanbo Wang, Quangao Qiu, Liangyu Feng, Jinhu Hu, Jianxin Shen, Xiao Wang, He Huang, Xinqi Zheng, Shiming Zhou, Baogen Shen, Shouguo Wang[*]

Pengwei Dou, Dr. Jingyan Zhang, Xiao Deng, Yuanbo Wang, Quangao Qiu, Liangyu Feng, Jinhu Hu, Dr. Jianxin Shen, Dr. Xiao Wang, Dr. He Huang, Dr. Xinqi Zheng, Prof. Shouguo Wang
School of Materials Science and Engineering, Key Laboratory of Advanced Materials and Devices for Post-Moore Chips, Ministry of Education, University of Science and Technology Beijing, Beijing 100083, China

E-mail: jyzhang@ustb.edu.cn, sgwang@ustb.edu.cn

Prof. Tao Zhu
Beijing National Laboratory for Condensed Matter Physics, Institute of Physics, Chinese Academy of Sciences, Beijing 100190, China

Dr. Peng Kang
School of Materials Science and Engineering, Beihang University, Beijing 100191, China

Prof. Shiming Zhou, Prof. Baogen Shen, Prof. Shouguo Wang
Anhui Key Laboratory of Magnetic Functional Materials and Devices, School of Materials Science and Engineering, Anhui University, Hefei 230601, China

Keywords: Spin orbit torque; fully electric controlling; canted ferrimagnets; spin absorption

[#]These authors contributed equally to this work.

Table of contents

Section S1: Magnetism of the Pt/Co/Gd(t_{Gd})/Ir multilayers

Section S2: Structural characterization of the Pt/Co/Gd(t_{Gd})/Ir multilayers

Section S3: PNR spectra of the Pt/Co/Gd(t_{Gd})/Ir multilayers

Section S4: Spin-dependent transport of the Pt/Co/Gd(t_{Gd})/Ir multilayers

Section S5: Co-Gd intermixing models at the Co/Gd interface

Section S1: Magnetism of the Pt/Co/Gd(t_{Gd})/Ir multilayers

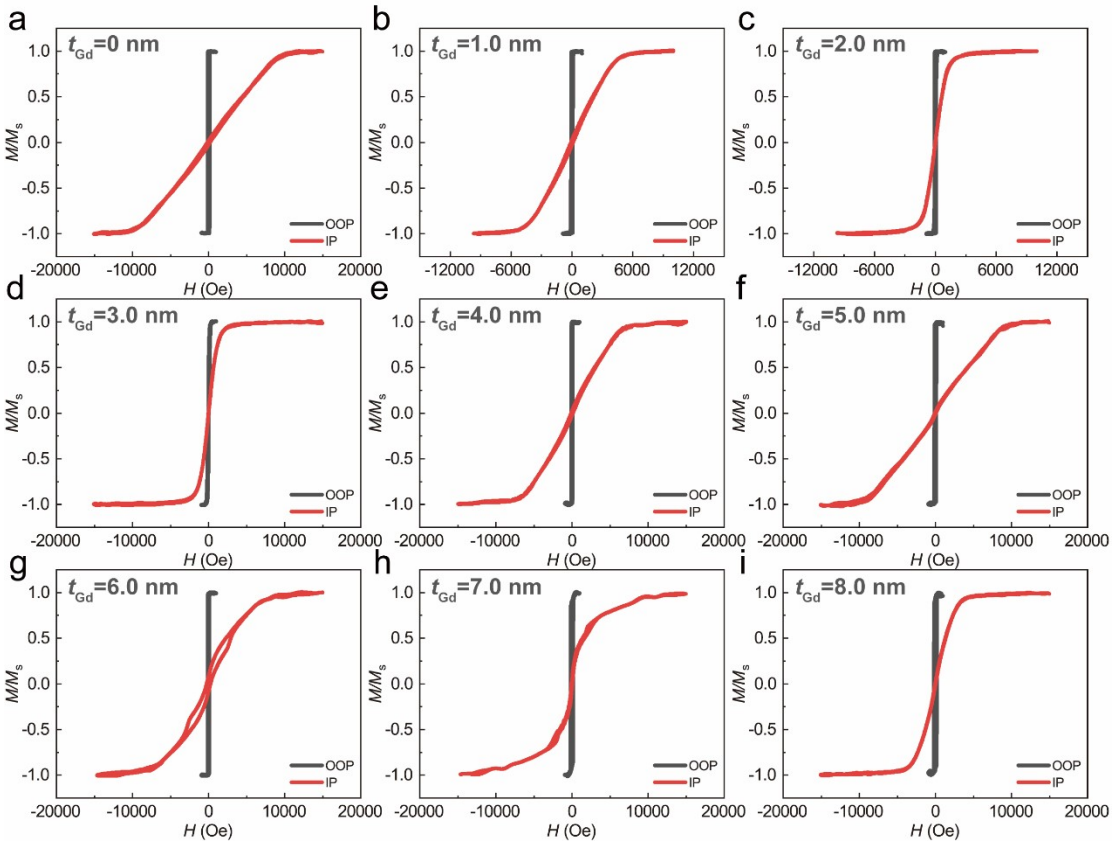

Fig. S1 (a)-(i) Normalized *M-H* loops of magnetic field perpendicular (black line) to and parallel (red line) to the thin film plane for Pt/Co/Gd(t_{Gd})/Ir multilayers, respectively.

Firstly, magnetic characterization was performed on the sputtered Pt/Co/Gd(t_{Gd})/Ir multilayers. The normalized magnetic hysteresis (*M-H*) loops of the magnetic field perpendicular (black line) to and parallel (red line) to the thin film plane are shown in Fig. S1. It can be seen that all multilayers are more prone to saturation in the out of plane (OOP) direction, and the enlarged *M-H* loops are the same as Fig. 1a. All of Pt/Co/Gd(t_{Gd})/Ir multilayers have good rectangles and 100% residual magnetization in the OOP direction, indicating that all samples have perpendicular magnetic anisotropy (PMA). In addition, the saturation magnetization M_s extracted from the *M-H* loops is shown in Fig. 1b, where M_s monotonically decreases with increasing t_{Gd}, indicating the antiferromagnetic coupling (AFMC) characteristics of Co and Gd in Pt/Co/Gd/Ir multilayers. To evaluate the magnetic compensation temperature (T_M) in Pt/Co/Gd(t_{Gd})/Ir, temperature dependent magnetic characterization was performed. As

shown in Fig. S2, the effective magnetization is 0 at 133 K and 173 K, only when t_{Gd} = 7 nm and 8 nm, respectively. Notably, the lowest point of the t_{Gd} = 6 nm M_s - T curve is not zero, with a value of 10 emu/cm^3. Accordingly, the T_M is much lower than room temperature, indicating that Co is dominant in Pt/Co/Gd(t_{Gd})/Ir multilayers.

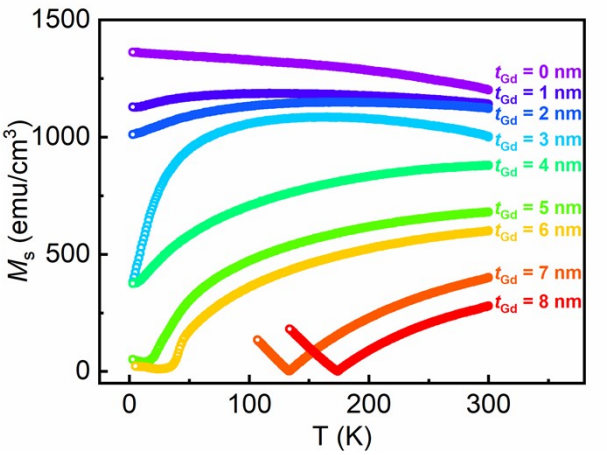

Fig. S2 The temperature dependent saturation magnetization M_s of Pt/Co/Gd(t_{Gd})/Ir (t_{Gd} = 0-8 nm) multilayers.

Section S2: Structural characterization of the Pt/Co/Gd(t_{Gd})/Ir multilayers

Thin films were processed into thin slices utilizing focusing ion beam (FIB) for transmission electron microscope (TEM) observation. Fig. S3a shows a high-resolution image of Pt/Co/Gd(5.0 nm)/Ir, where Pt, Co, Gd and Ir exhibits obvious layering and smooth interface, indicating that the grown sample is consistent with the nominal design. In addition, it can be qualitatively observed that the Pt, Co, and Ir layers have clear lattice patterns, while the Gd layer does not. Combining the fast Fourier transform (FFT) in the corresponding Pt/Co and Gd regions, as shown in Fig. S3b and S3c, the dispersed rings and hexagonal lattice imply that Pt, Co and Ir has fine crystallinity while Gd is amorphous. The high-resolution high-angle annular dark field scanning transmission electron microscopy (HR HAADF-STEM) image of Pt/Co/Gd(5.0 nm)/Ir is shown in Fig. S4a, where bright and dark regions represent the Pt and Ir layers with larger atomic numbers, as well as the Co and Gd layers with smaller atomic numbers, respectively. In addition, the obvious lattice fringes were also observed in the bright

regions, which is consistent with TEM results. Fig. S4b demonstrates the depth distribution of Pt L_α (pink line), Co K_α (blue line), Gd L_α (red line) and Ir L_α (yellow line) along the white arrows (Energy dispersive X-ray spectroscopy, EDS). It can be clearly seen that the distribution of the Pt, Co, Gd and Ir elements is concentrated in different positions, which is consistent with the qualitative observation of TEM (Fig. 1c and S3a), further indicating the reliability of sample growth. Similarly, the results of element depth analysis using X-ray photoelectron spectroscopy (XPS) are shown in Fig. S5b. In addition, as shown in Fig. S5c and S5d, the high-resolution XPS spectra of Pt 4f and Co 2p at the Pt/Co interface indicate that the sputtered Pt/Co/Gd(t_{Gd})/Ir multilayers are metallic.

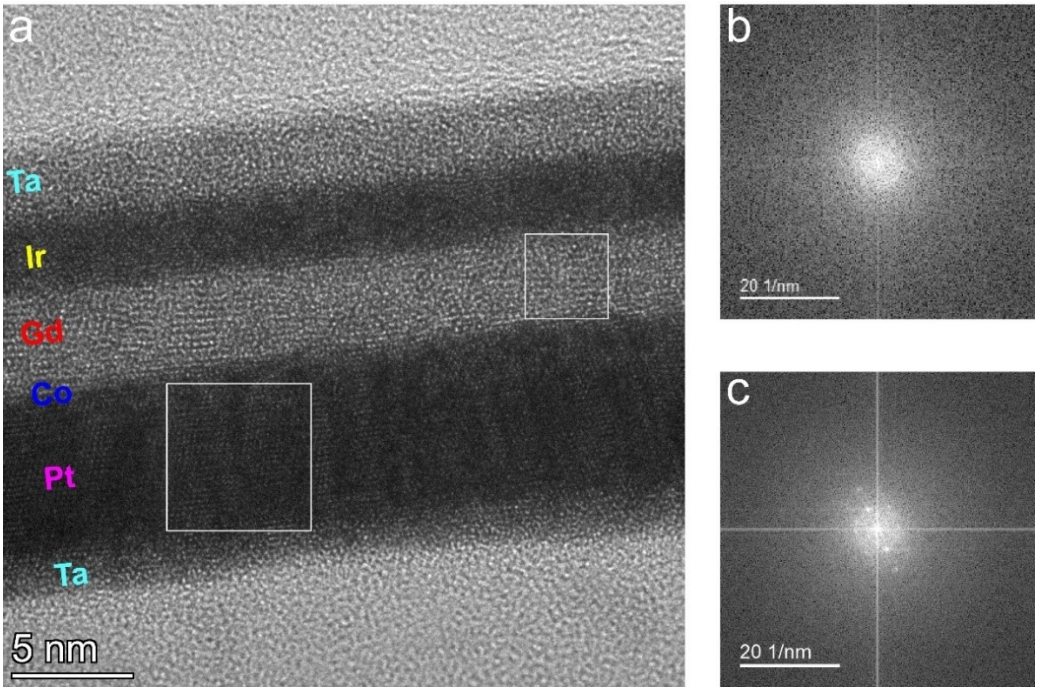

Fig. S3 (a) HR-TEM image of Pt/Co/Gd(5.0 nm)/Ir multilayers, where different colored fonts represent different layers. Fast Fourier transform images of Pt/Co (b) and Gd (c) regions marked by white square.

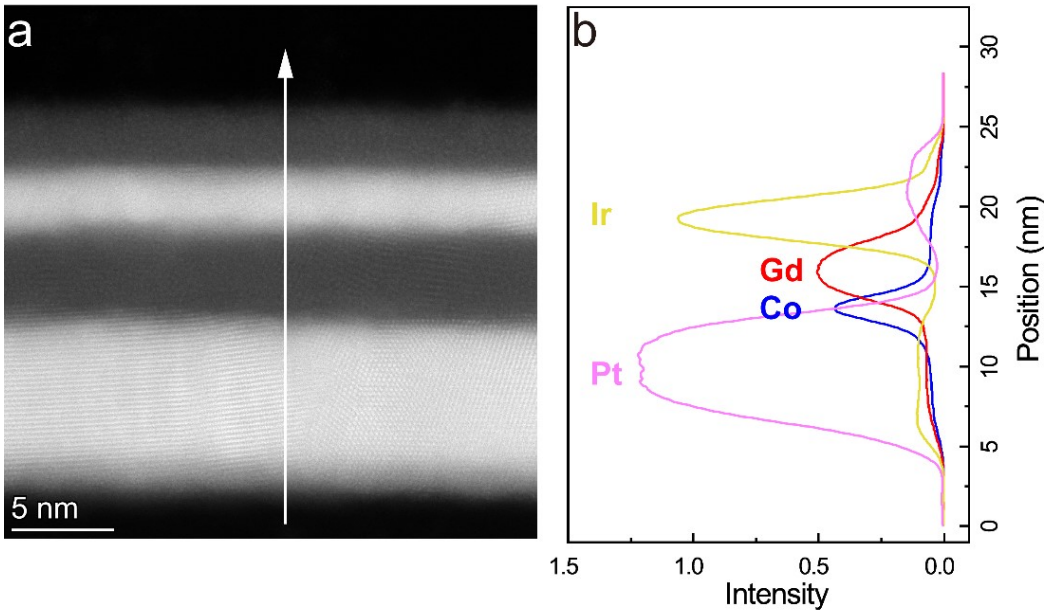

Fig. S4 (a) HR HAADF-STEM image of Pt/Co/Gd(5.0 nm)/Ir multilayers. (b) Depth distribution of Pt L_α (pink line), Co K_α (blue line), Gd L_α (red line) and Ir L_α (yellow line) along the white arrow in (a).

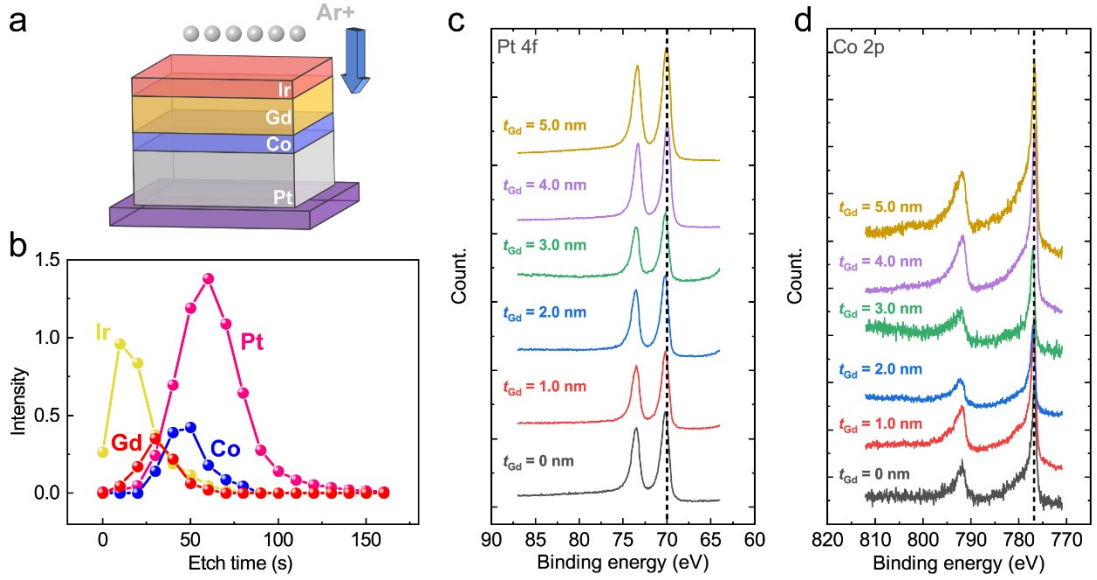

Fig. S5 (a) Schematic diagram of XPS with depth analysis. (b) The content variation of Pt (pink line), Co (blue line), Gd (red line) and Ir (yellow line) element with etching time. (c) Pt 4f and (d) Co 2p HR-XPS spectra at Pt/Co interface in Pt/Co/Gd(t_{Gd})/Ir multilayers.

Section S3: PNR spectra of the Pt/Co/Gd(t_{Gd})/Ir multilayers

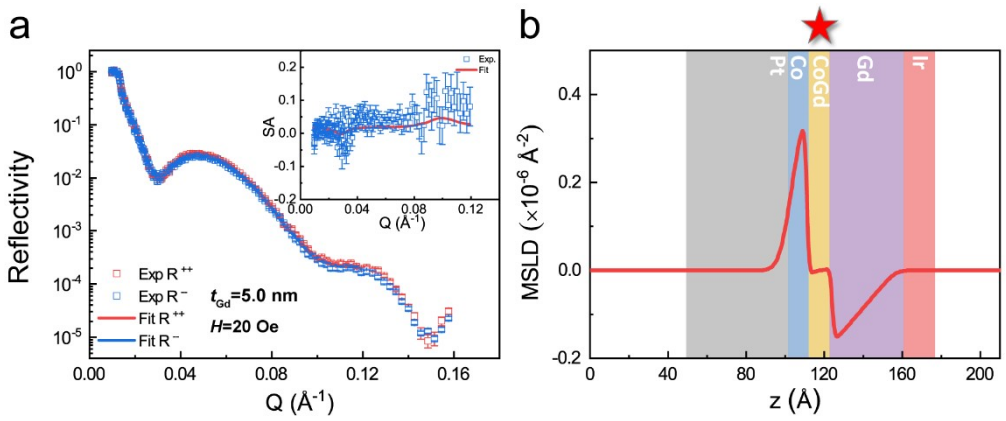

Fig. S6 (a) The R^{++} and R^{--} reflectivity vs. scattering vector Q under 20 Oe for Pt(5.0)/Co(1.0)/Gd(5.0)/Ir(2.0) (in nm). Insets are the corresponding spin asymmetry (SA). (b) Depth distribution of magnetic scattering length density (M-SLD, red line), where the gray, blue, yellow, purple and red areas represent Pt, Co, CoGd, Gd and Ir layers respectively.

The momentum transfer (Q)-dependent reflectivity curves for Pt/Co/Ir trilayers with 1.0 nm Gd insertion is shown in Fig. S7a, where the in-plane magnetic field is 12000 Oe. It is visible that the reflectivity curves of R^{++} (red squares) and R^{--} (blue squares) are different originating from different magnetic scattering events of neutrons with spin-up and spin-down. The depth of structure (Nuclear scattering length density, N-SLD, black line) and magnetizations (Magnetic scattering length density, M-SLD, red line) can be extracted from Q-dependent reflectivity curves, as shown in Fig. S7c. Notably, consistent with the t_{Gd} = 5.0 nm, t_{Gd} = 1.0 nm exhibits three platforms in the M-SLD, further confirming that spontaneous CoGd layer is credible. In addition, the tilting angle of the magnetic moment in multilayers with perpendicular magnetic anisotropy can be accurately characterized by PNR under different magnetic fields. For multilayers with PMA, an in-plane magnetic field of 20 Oe is not sufficient to affect the orientation of the magnetic moment, but it is necessary for neutron polarization. Therefore, the PNR result under 20 Oe can be approximated as the ground state of the multilayers. As shown in Fig. S7b, the reflectivity curves of R^{++} (red squares) and R^{--} (blue squares) under 20 Oe are overlapped, owing to most of magnetic moments perpendicular to film plane. More importantly, non-zero spin asymmetry (SA), defined as $(R^{++}-R^{--})/(R^{++}+R^{--})$

corresponding to Fig. S7b manifests that the magnetic moment of Pt/Co/Gd/Ir is canted in the ground state. The titling angles of Co, CoGd, and Gd in Pt/Co/Gd(1.0 nm)/Ir multilayers can be determined as 1.1°, 5.9°, and -17°, respectively. Particularly, the opposite angle for Co and Gd layer in Pt/Co/Gd/Ir further reveals the antiparallel magnetizations, which is consistent with magnetism results.

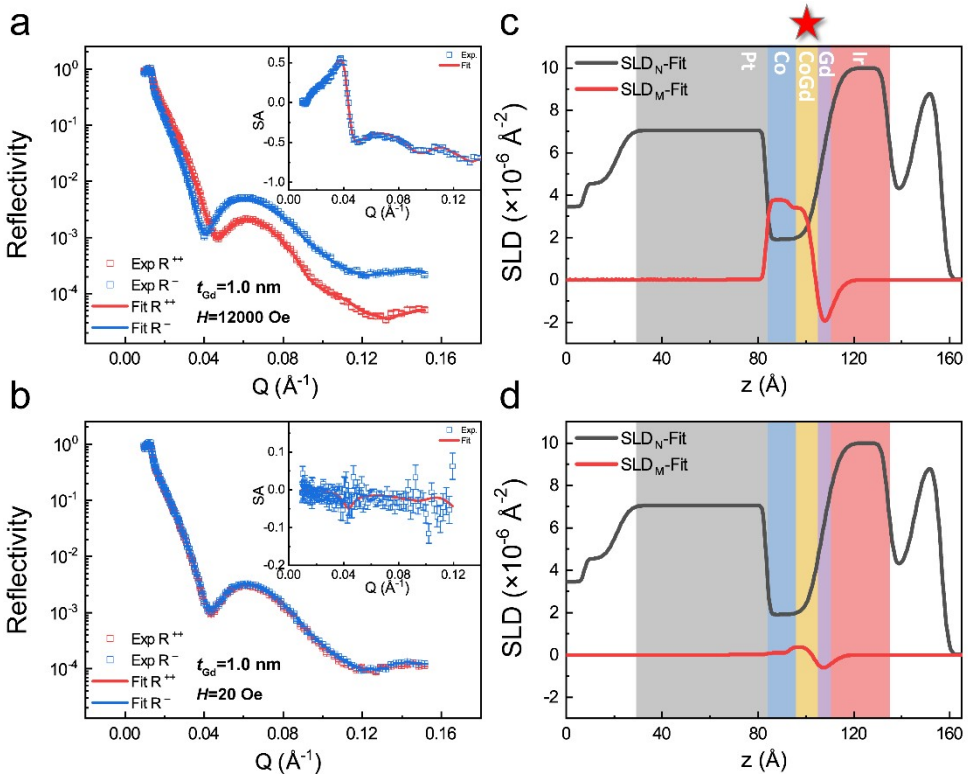

Fig. S7 The R^{++} and R^{--} reflectivity vs. scattering vector Q under 12 kOe (a) and 20 Oe (b) of Pt/Co/Gd(1.0 nm)/Ir, respectively. Depth distribution of magnetic scattering length density (M-SLD, red line) and nuclear scattering length density (N-SLD, black line) under 12 kOe (c) and 20 Oe (d), where the gray, blue, green, yellow and red areas represent Pt, Co, CoGd, Gd and Ir layers respectively.

Section S4: Spin-dependent transport of the Pt/Co/Gd(t_{Gd})/Ir multilayers

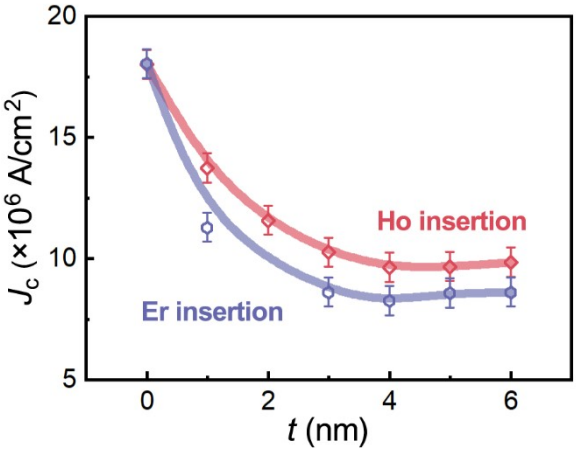

Fig. S8 The J_c of SOT-driven magnetization switching vs. thickness in various rare-mental insertion. The red diamond and the purple hexagon represent Ho and Er insertion, respectively.

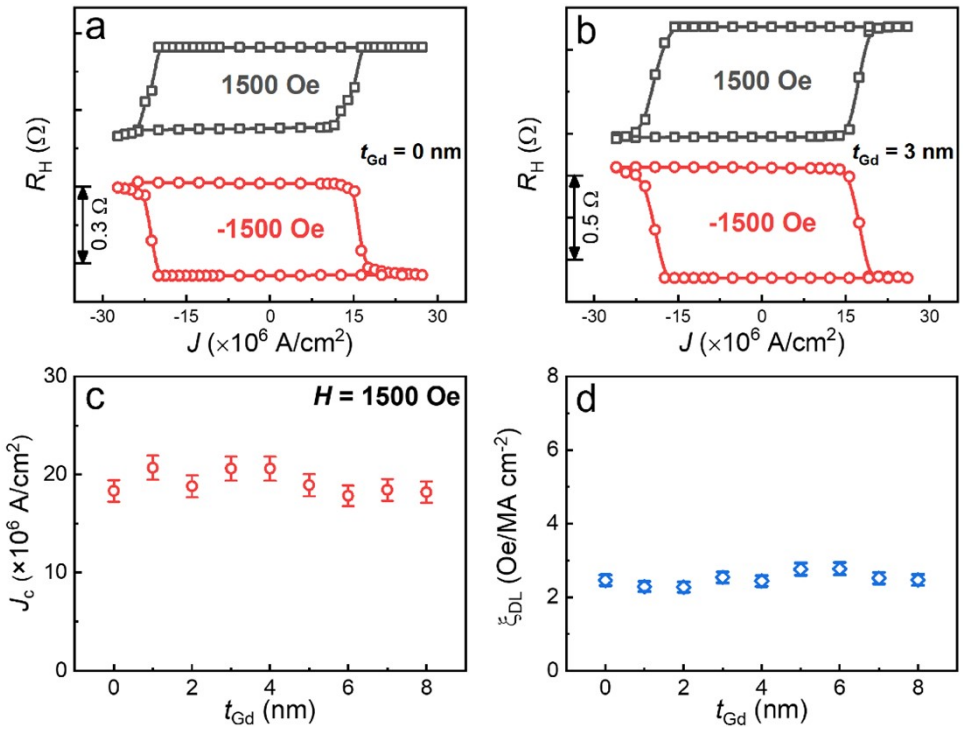

Fig. S9 SOT-driven magnetization switching executed with H_x = ±1500 Oe for Pt/Co/Ir/Gd(0 nm) (a) and Pt/Co/Ir/Gd(3 nm) (b) multilayers. (c) The J_c of SOT-driven magnetization switching vs. t_{Gd} in Pt/Co/Ir/Gd(t_{Gd} = 0-8 nm) multilayers. (d) The H_{DL} per unit current density ($\xi_{DL} = H_{DL}/J$) as function of t_{Gd} for Pt/Co/Ir/Gd(t_{Gd}) multilayers.

In order to test the universality of reducing J_c by the insertion of rare-metals, current driven magnetization switching was performed on multilayers with various rare

metals, and the extracted critical switching current density as function of thickness are shown in Fig. S8. Consistent with the results of Pt/Co/Gd/Ir, J_c sharply decreases with the increase of Ho (red diamond) and Er (purple hexagon) thickness. When the thickness reaches 4.0 nm, J_c reaches a minimum value. For comparison, current-driven magnetization switching and harmonic measurements were performed in Pt/Co/Ir/Gd(t_{Gd}) multilayers, where Co and Gd are separated by Ir layers. As shown in Fig. S9c and S9d, the J_c and ξ_{DL} of Pt/Co/Ir/Gd with t_{Gd} remain, which indicates that the FM/RM interface has a significant impact on SOT-dependent transport. In addition, SOT-driven magnetization switching was performed on Pt/Co/Gd/Ir multilayers with different t_{Gd} at different temperatures, as shown in Fig. S10a (t_{Gd} = 0 nm) and S10b (t_{Gd} = 3.0 nm). Among them, it can be qualitatively observed that as the temperature decreases, with or without 3.0 nm Gd, the critical switching current density J_c gradually increases, which is attributed to the increase in switching potential barrier caused by lower temperature. Fig. S10c summarizes the temperature dependence of J_c extracted from Fig. S10a and S10b, where red and blue balls represent t_{Gd} = 0 nm and 3.0 nm, respectively. It is worth noting that the introduction of Gd increases the temperature resistance of spin-dependent transport, that is, the lower temperature makes the increase in J_c less significant compared to the absence of Gd. To quantitatively describe the temperature dependence of spin-dependent transport, the slope of the curve in Fig. S10c is defined as $k = |\Delta J_c/\Delta T|$. For Pt/Co/Gd(0 nm)/Ir, $k = 0.0064$, while $k = 0.0037$ for Pt/Co/Gd(3.0 nm)/Ir which is almost half of without Gd. In general, during the magnetization switching process driven by SOTs, the critical switching current density J_c can be expressed as:

$$J_c = \frac{2e}{\hbar}\frac{M_s t_{FM}}{\theta_{eff}}\left(\frac{H_k}{2} - \frac{H_x}{\sqrt{2}}\right) = \frac{1}{\xi_{DL}}\left(\frac{H_k}{2} - \frac{H_x}{\sqrt{2}}\right)$$

It can be seen that J_c is mainly affected by SOT efficiency (ξ_{DL}), anisotropic field (H_k), and external magnetic field (H_x). As the temperature decreases, H_k monotonically increases in HM/FM multilayers, leading to an increase of J_c. A small k value indicates

a negligible temperature dependence of spin transport in Pt/Co/Gd/Ir multilayers, indicating strong temperature stability which has great significance for the application of spin-related devices.

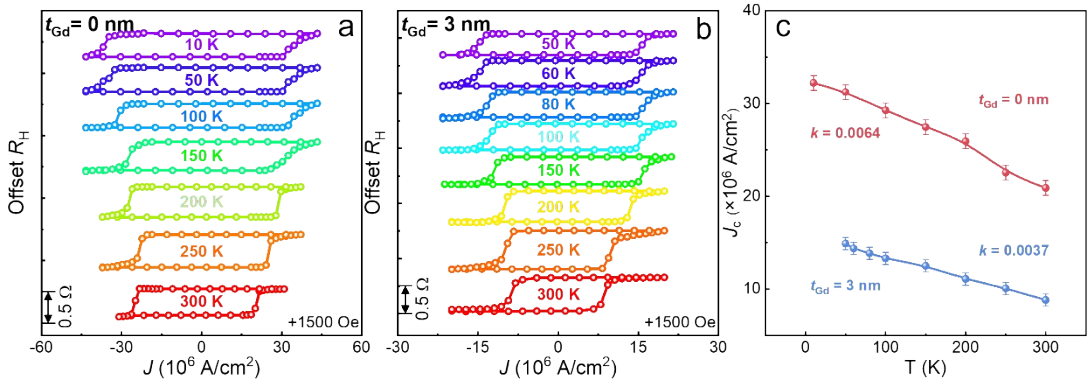

Fig. S10 SOT-driven magnetization switching executed under various temperature with H_x = +1500 Oe for Pt/Co/Gd(0 nm)/Ir (a) and Pt/Co/Gd(3.0 nm)/Ir (b) multilayers. (c) J_c extracted from (a) and (b) as a function of temperature, where k is the corresponding slope of linear fitting.

Fig. S11a, S11b, and S11c show the SOT-driven magnetization switching under various applied magnetic fields H_x at room temperature for Pt/Co/Gd(1.0 nm)/Ir, Pt/Co/Gd(2.0 nm)/Ir, and Pt/Co/Gd(4.0 nm)/Ir, respectively. Under a positive magnetic field (+H_x), the polarity of magnetization switching is counterclockwise, while under a negative magnetic field (-H_x), the polarity of magnetization switching is clockwise, which is consistent with the results of t_{Gd}=0 and 3.0 nm (Fig. 2d and 2e), indicating that Pt is the source of spin current in Pt/Co/Gd/Ir multilayers. Importantly, field-free magnetization switching is realized for t_{Gd}=1.0 and 2.0 nm, with the same polarity for t_{Gd}=3.0 nm and the opposite polarity for t_{Gd}=0 nm, indicating that with and without Gd layer has opposite H_{eff}.

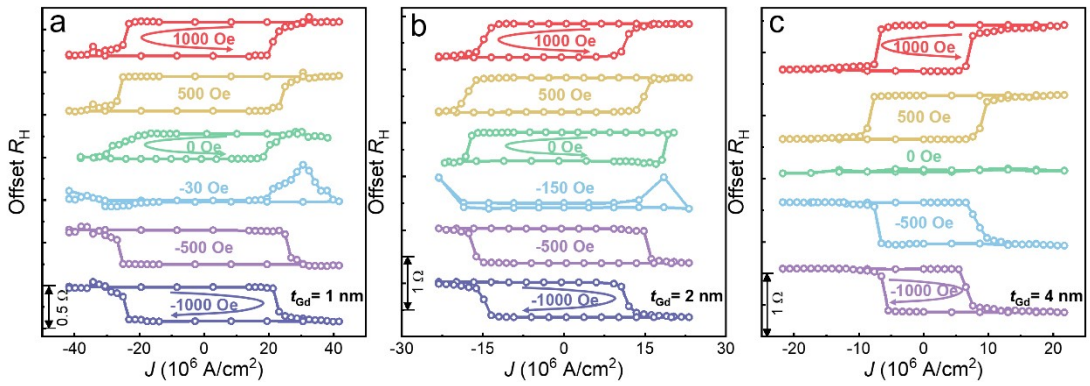

Fig. S11 SOT-driven magnetization switching loops measured under various H_x at room temperature for Pt/Co/Gd(1.0 nm)/Ir (a), Pt/Co/Gd(2.0 nm)/Ir (b) and Pt/Co/Gd(4.0 nm)/Ir (c) multilayers.

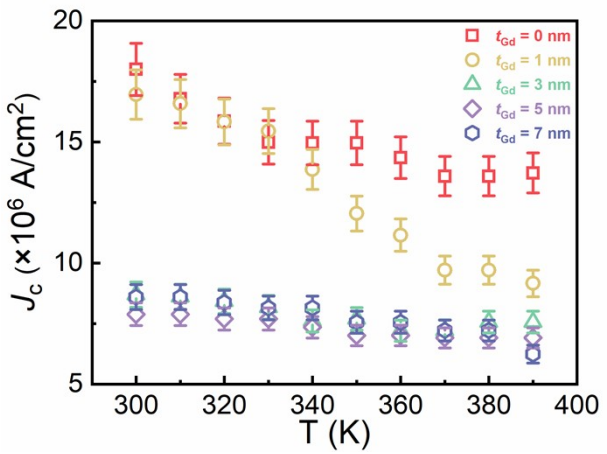

Fig. S12 SOT-driven magnetization switching loops measured above 300 K with H_x = +1500 Oe for Pt/Co/Gd(t_{Gd})/Ir multilayers, where the square, circle, triangle, diamond, and hexagon represent t_{Gd} = 0, 1, 3, 5, 7 nm, respectively.

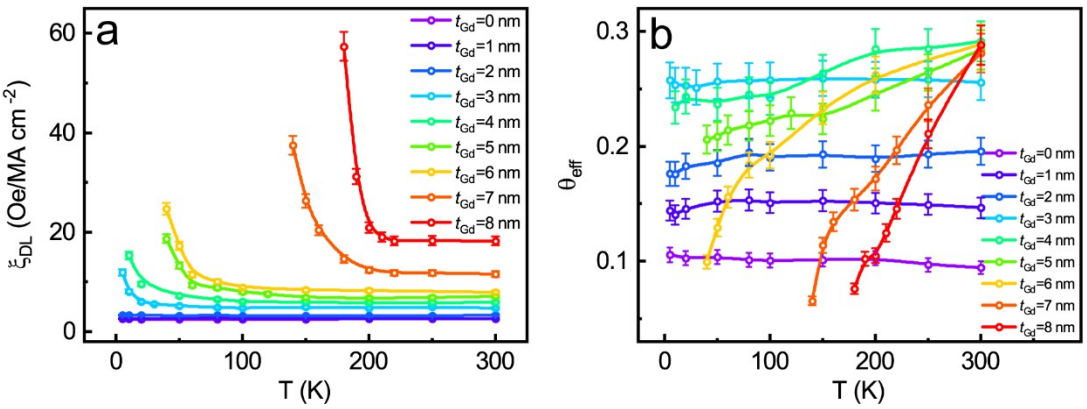

Fig. S13 The temperature dependent ξ_{DL} (a) and calculated spin Hall angle θ_{eff} (b) with temperature for Pt/Co/Gd(t_{Gd})/Ir (t_{Gd} = 0-8 nm) multilayers.

As shown in Fig. S12, SOT-driven magnetization sswitching was performed above 300 K, where J_c did not change dramatically with temperature, only slightly decreased, thus excluding the anomalous thermal-assisted J_c reduction. In addition, the ξ_{DL} and θ_{eff} with temperature are shown in Fig. S13a and S13b, respectively. It can be seen that when $t_{Gd} \leq 4$ nm, the θ_{eff} does not change significantly with temperature. While

when $t_{Gd} > 4$ nm, the θ_{eff} monotonically decreases with decreasing temperature, which can be attributed to a decrease in the rate of spin transfer to magnetization compared to the rate of spin relaxation owing to spin-orbit scattering.

Section S5: Co-Gd intermixing models at the Co/Gd interface

In order to investigate the improvement of SOT efficiency caused by spontaneous mixing at Co/Gd interface, first principles calculations using the Keldysh non-equilibrium Green's function (NEGF) combined with density functional theory (DFT) were executed to analyze the interfacial spin mixing conductance. The system used for the calculation contains Co as well as Gd atoms, where the scattering region consists of six layers of Co and Gd. Fig. S14 demonstrates the Co-Gd intermixing model at Co/Gd interface, Model 1-Model 8. Model 1 is the pristine state without intermixing. Model 2-4 and Model 5-8 are Co-Gd intermixing in one-layer and two-layers respectively. The calculated spin mixed conductivity ($G_r^{\uparrow\downarrow}$) of different models is summarized in Fig. 5c.

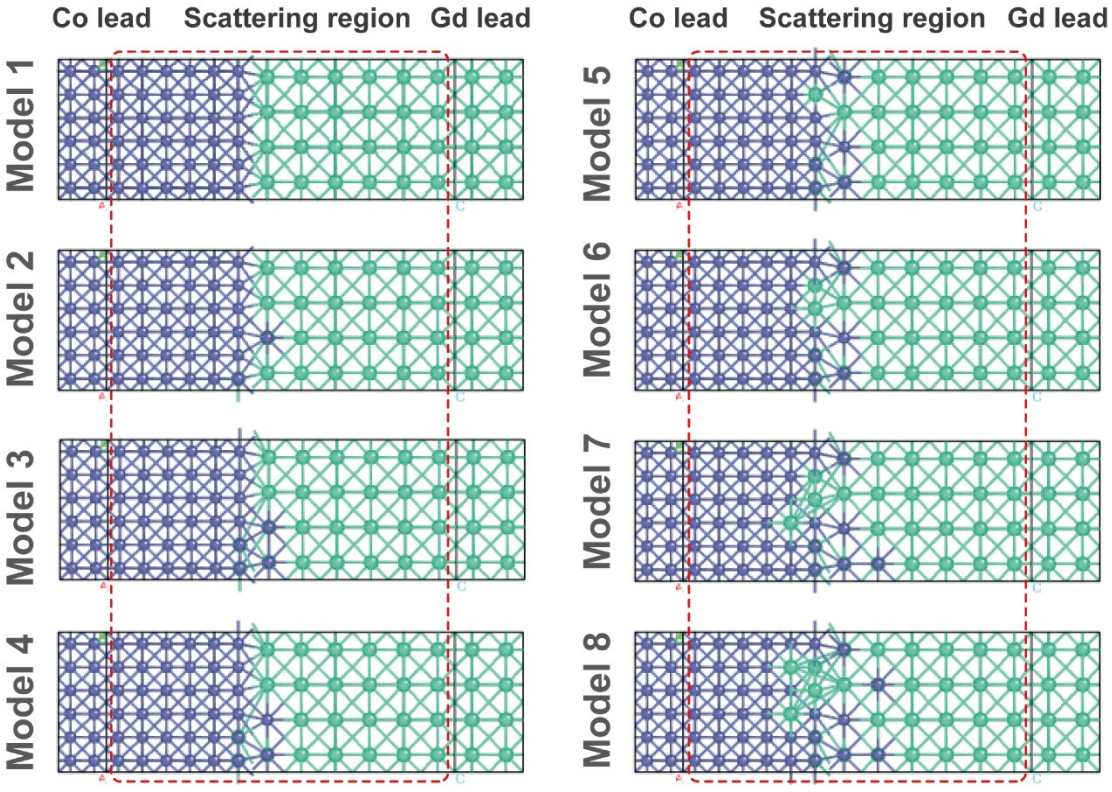

Fig. S14 Various Co-Gd intermixing model at Co/Gd interface, where the green and blue balls represent Gd and Co atoms, and the red dotted squares are scattering region.